**Rare Metal Materials and Engineering**
Volume 54, Issue 12, December 2025
Available online at www.rmme.ac.cn

Science Press

**Cite this article as**: Wang Yingdi, Zhang Guiqing, Yang Taisen, et al. Microstructure Evolution Characteristics and Mechanical Properties of a Novel Nitrogenous Nickel-Based Deposited Metal from Gas Metal Arc Welded State to Heat-Treated State[J]. Rare Metal Materials and Engineering, 2025, 54(12): 3010-3023. DOI: https://doi.org/10.12442/j.issn.1002-185X.20240744.

ARTICLE

# Microstructure Evolution Characteristics and Mechanical Properties of a Novel Nitrogenous Nickel-Based Deposited Metal from Gas Metal Arc Welded State to Heat-Treated State

**Wang Yingdi[1,2], Zhang Guiqing[1], Yang Taisen[1], Liang Xuewei[1], Su Yunhai[1]**

*[1] School of Materials Science and Engineering, Shenyang University of Technology, Shenyang 110870, China; [2] Department of Transportation Engineering, Yantai Vocational College, Yantai 264670, China*

**Abstract:** A novel nitrogenous nickel-based deposited metal was prepared by gas metal arc welding. Subsequently, solid solution treatment as well as solution and aging treatments were conducted on the prepared metal to study the evolution of microstructure and tensile properties at different states. Results show that the high-temperature tensile strength of the deposited metal exhibits good performance after the addition of W and N. The grain size of the sample is large, and petal-like Laves phase appears at the grain boundaries. After solid solution treatment, the grain size decreases, and the Laves phase disappears. However, both the yield strength and elongation of the deposited metal decrease. The grain size of the samples after solid solution and aging treatment is more uniform, nanoscale $M$(C, N) phases are precipitated within the crystals, and $M_{23}C_6$ phase forms at grain boundaries. The yield strength and ultimate tensile strength of this sample are higher than those of the other samples, but its plasticity is the lowest. The main deformation mechanism is the unit dislocation $a/2<110>$ cutting the precipitation phase.

**Key words:** nitrogenous deposited metals; microstructure; tensile performance; dislocation

## 1 Introduction

Ultra-supercritical power generation unit, as an efficient and environmentally friendly choice for future power generation, attracts much attention nowadays. The commonly used materials for ultra-supercritical power generation units are iron-based and nickel-based alloys. The nickel-based alloys have high-temperature resistance and corrosion resistance, so they can serve safely in high-temperature and high-pressure environments. At present, the most popular operating unit is the 600 ℃ ultra-supercritical power generation unit. There are many types of nickel-based superalloys, which are considered as the preferred materials to weld the advanced ultra-supercritical (AUSC) boilers due to their excellent corrosion resistance, oxidation resistance, as well as good tensile and fatigue properties[1]. AUSC boiler is composed of components of various materials. Therefore, the advanced austenitic steels need to be welded with the nickel-based superalloys. Inconel 625 alloy exhibits excellent mechanical properties from low temperature to 980 ℃. Inconel 625 filler wire can adapt to differences in chemical composition and thermal expansion between different metals, which is suitable for welding different metals[2–3] and can significantly improve the high-temperature mechanical properties of welded joints[4–5]. However, the continuous rise in nickel ore price leads to a constant increase in the cost of nickel-based welding materials. Therefore, it is necessary to develop a new type of low-cost welding materials with excellent performance. Nickel-based alloys are typical solid solution-strengthened superalloys. Thus, transition group elements, such as Mo, Co, Nb, and Hf, have been added to the nickel-based welding materials to enhance the strength. At the

Received date: December 18, 2024
Corresponding author: Su Yunhai, Ph. D., Professor, School of Materials Science and Engineering, Shenyang University of Technology, Shenyang 110870, P. R. China, E-mail: su_yunhai@sut.edu.cn

same time, a certain amount of transition element W has also been added to the nitrogenous nickel-based welding materials. Transition group elements can improve the mechanical properties of alloys at high temperatures, because they can not only reduce the diffusion ability of other alloying elements, but also lower the stacking fault energy of the alloy[6–10]. The presence of refractory alloy element W and boundary strengthening element C can provide high thermal fatigue resistance for the alloy and have beneficial effects[11]. With the addition of element Ti, nanostructured W-Ti forms and exhibits significant high-temperature stability[12]. Nitrogen has a strong stabilizing effect on austenite. Therefore, adding nitrogen to the alloys can improve the strength of austenitic stainless steel[13]. The presence of nitrogen can lead to the formation of carbonitrides in alloys, which are more stable than carbides[14]. Thus, these elements have a very positive effect on the high-temperature creep resistance of nickel-based alloys.

The precipitates in the nickel-based superalloys usually include $\gamma'$ phase, carbide phase, $\delta$ phase, and Laves phase. These residues also have a significant impact on the properties of alloy. Liu et al[15] studied the effect of long-term thermal exposure on the microstructure and stress-rupture properties of GH3535 superalloy. They found that cracks originated from the interface between $M_6C$ carbides and the matrix, resulting in a lower creep fracture life. He et al[16] found that grain boundaries could promote the precipitation of $M_{23}C_6$, and the small $M_{23}C_6$ located at the grain boundary could strengthen the boundary and effectively prevent grain boundary migration. It was found that the formation of the $\gamma'$ phase promotes the transformation of *M*C phase to the $M_{23}C_6$ phase[17]. Microcracks can form near or inside the *M*C degradation zone and are detrimental to the high-temperature strength of the alloy, especially when *M*C is present at the grain boundary[18]. The Laves phase in nickel-based superalloys is called the undesired phase. The segregation of the Laves phase will consume a large number of solid solution strengthening elements in the alloy, thereby reducing the high-temperature strength of the alloy. Post-treatment, such as heat treatment, is an effective method to eliminate the harmful Laves phases[19]. In addition, the distribution and size of the $\gamma'$ phase have a considerable impact on the tensile strength of nickel-based alloys at elevated temperatures[20]. Besides, solid solution treatment also has a significant impact on the properties of nickel-based alloys. Abolfazl et al[21] studied the properties of Inconel 625 alloy fabricated by the gas metal arc welding (GMAW) method and found that solution heat treatment reduced the elongation of the alloy but increased its hardness and yield strength. Mathieu et al[22] studied the characteristics of nickel-based alloys produced by the laser-powder bed fusion method at different states and found that the microstructure of the alloys changed obviously after various heat treatment methods. Wang et al[23] found that by controlling the heat treatment temperature, the grain size, grain boundary characteristics, and dislocation density of the alloy could be adjusted, thereby affecting the mechanical properties of the alloy. Mostafaei et al[24] reported that aging treatment could improve the microhardness and tensile strength of the sample, but reduce the plasticity.

In this research, a certain amount of elements N and W was added into Inconel 625 welding material, and the contents of elements Fe and Mn were increased to obtain a nickel-based alloy with lower cost and good mechanical properties. This novel type of welding material was denoted as nitrogenous nickel-based flux-cored welding wire. The microstructure and mechanical properties of this nitrogenous nickel-based flux-cored wire-deposited metal under different conditions were investigated. This study provided reliable data to support the design of low-cost alloys for ultra-supercritical material applications.

## 2 Experiment

Inconel 625 welding material was used in this experiment and JMatPro software was used for composition design. The nitrogenous nickel-based flux-cored wire used in this experiment was 1.2 mm in diameter, and the optimal chemical composition was 0.10wt% C, 2.50wt% Mn, 0.45wt% Si, 0.20wt% Cu, 41.00wt% Ni, 1.30wt% Ti, 1.50wt% Al, 22.00wt% Cr, 4.50wt% Mo, 5.00wt% Nb, 4.00wt% W, 0.55wt% N, <0.001wt% P, <0.001wt% S, and balanced Fe. The material was deposited layer by layer on 304L stainless steel plate with a YD-500FR2 gas-shielded welding machine. Each layer was deposited in the opposite direction to that of the previous one with an interval of 3 min between passes to control the temperature between different passes not exceeding 150 °C. In addition, the protective gas is composed of 97vol% argon and 3vol% nitrogen, which inhibits weld metal oxidation during welding. The deposition parameters of the overlays were welding current of 180 A, welding speed of 25 cm/min, and welding voltage of 25 V. Thereafter, walls of four overlay welding passes with 180 mm in length and 12 mm in height were fabricated. The as-deposited samples were denoted as AD samples. Three walls at different states were fabricated, and the schematic diagram of wall is shown in Fig.1.

In order to find the exact solution treatment temperature, differential scanning calorimetry (DSC) test was conducted on the prepared samples. A cylindrical DSC sample was cut off from the deposited metal by wire-cutting machine, and the oxide scale on the surface was removed by sandpaper and cleaned by ultrasonics for 5 min. The instrument used in this experiment is THEMYS comprehensive analyzer with a protective atmosphere of argon gas with flow rate of 20 mL/min.

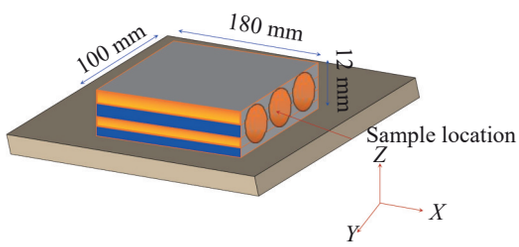


Fig.1 Schematic diagram of deposition path

The processed sample was placed in an alumina dry pot with the testing temperature range of 800–1400 ℃ and heating rate of 10 °C/min.

To obtain a homogeneous microstructure, AD samples were solution heat-treated in an electric furnace at 1080±5 ℃ for 4 h and then quenched in water, and these samples are denoted as ST samples. Subsequently, the samples were aged at 700 ℃ for 24 h and then air cooled, and these samples were denoted as SA samples. The heating rate of the solid solution treatment was 10 and 2 ℃/min below and above 600 ℃, respectively. To investigate the effect of heat treatment on the mechanical properties of the alloys, high-temperature tensile tests were conducted on AD, ST, and SA samples. Tensile tests were performed on MST Landmark 370.10 microcomputer-controlled electro-hydraulic servo tester at 600 ℃. The samples were heated to the designed temperature at heating rate of 1 ℃/s and held at designed temperature for 10 min. Then, the test was conducted at a constant tensile rate of 0.1 mm/min until the sample fractures. The schematic diagram of the stretching device is shown in Fig.2.

The phase composition of AD sample was characterized by X-ray diffractometer (XRD, model XRD − 7000) and the scanning range was 20° – 100°. AD sample was chemically etched with aqua regia ($HCl:HNO_3$=3:1) at room temperature for 20 s to observe the microstructure features. Tensile fracture morphology was observed using the BX60M optical microscope (OM) and scanning electron microscope (SEM), while the microstructure and element analyses were performed using a field emission SEM (GeminiSEM-300) coupled with energy dispersive spectroscope (EDS). The microstructure and dislocation morphology of different samples were observed using the JEM-2100 transmission electron microscope (TEM). The crystal orientation was analyzed using electron backscattered diffractometer (EBSD), and the average grain size was calculated by Oxford-HKL Channel 5 software.

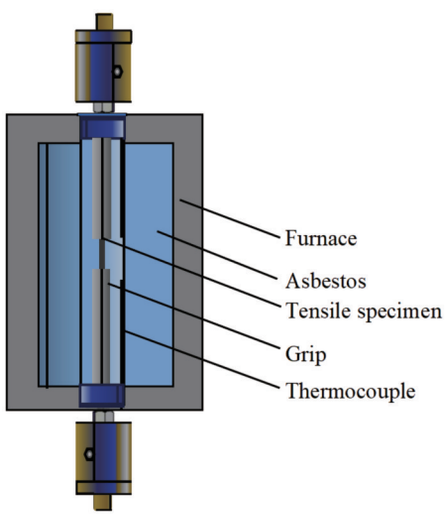


Fig.2 Schematic diagram of tensile testing device

## 3 Results

### 3.1 Phase constituents

The phase transition temperatures of AD samples were determined by DSC, and the resultant DSC curves are shown in Fig. 3. According to the heating curve in Fig. 3a, four distinct thermal reaction zones can be observed. The first reaction region has a lower temperature and a smaller area. Based on the intensity and location of the thermal reaction region, this thermal reaction region corresponds to the reaction of solid dissolution of the carbide phase in the $\gamma$ matrix (896 °C). The second thermal reaction is more intense, which happens at the transformation temperature from solid phase into liquid phase in the alloy, namely the initial melting temperature of the alloy (1121 ℃). The solidus temperature obtained using the initial temperature extrapolation method is approximately 1223 ℃, indicating that the matrix begins to melt. The third pronounced thermal reaction region is related to the endothermic reaction during the solid solution of carbonitrides (1242 ℃). The intensity of the fourth endothermic peak is the most pronounced, indicating that this reaction is the most dominant endothermic reaction during the entire heating process, which corresponds to the melting temperature of the $\gamma$ phase (1264 ℃).

Fig.3b shows DSC cooling curve. Four distinct exothermic peaks can also be observed. The first exothermic peak is

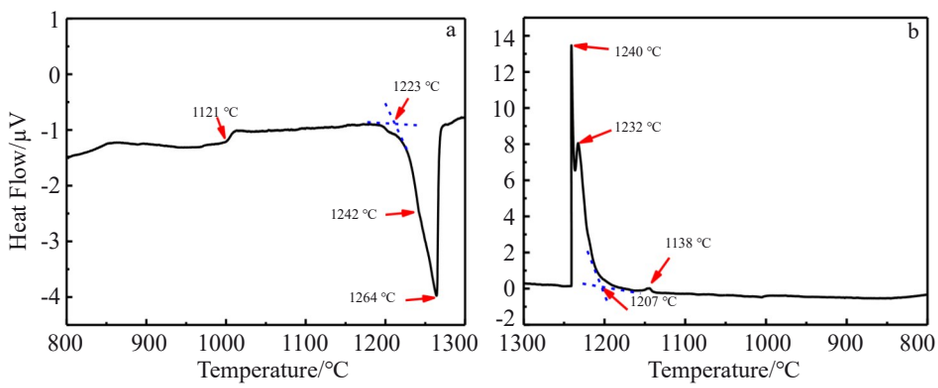


Fig.3 DSC results of AD samples: (a) heating curve and (b) cooling curve

related to the most important exothermic reaction during solidification, which represents the precipitation temperature of the primary $\gamma$ phase. The second exothermic peak corresponds to the precipitation reaction of carbon and nitride in AD sample. The third exothermic peak represents the precipitation of the Laves phase. The magnitude of this peak area indirectly reflects the Laves phase content. The fourth exothermic peak represents the precipitation of the carbide phase.

The high-temperature metallographic method was used to further confirm the initial melting temperature of AD sample. As shown in Fig.4b, a tiny melt pool appears in AD sample at 1120 ℃, indicating that the initial melting of the low-melting-point eutectic organization in the alloy occurs, but the melt pool does not appear at 1115 ℃ (Fig.4a). Therefore, it can be determined that the initial melting temperature of AD sample is around 1115 ℃. In order to improve the efficiency of the solution treatment as much as possible and to avoid the initial melting, considering the temperature fluctuation of the furnace during the solution treatment and other factors, the solution treatment temperature of AD sample is set to 1110 ℃.

XRD patterns of AD, ST, and SA samples are shown in Fig. 5. It can be seen that all samples consist of $\gamma$ solid solution phase with face-centered cubic structure (PDF#33-0397 standard card), which corresponds to (111), (200), and (311) diffraction peaks. The diffraction intensity of the (200) peak is much higher than that of other peaks, indicating that the grains grow along the <200> preferential orientation. In addition, the carbon-nitride phase appears in all three samples. The Laves phase only exists in AD sample. XRD patterns can provide a preliminary judgement on the phase structure of the alloys, but the constituent elements and proportions of the structures of crystal structures with similar lattice constants ($\gamma$ and $\gamma'$) can hardly be determined accurately.

### 3.2 Tensile behavior

Fig. 6 shows the tensile engineering stress-engineering strain curves, and the corresponding tensile property results are shown in Table 1. The tensile stress remains constant until the samples fracture, and all three samples exhibit significant work-hardening behavior after yielding. The yield strength, ultimate tensile strength, and elongation of AD sample is 456.51 MPa, 689.01 MPa, and 26.81%, respectively. The yield strength and ultimate tensile strength of SA sample are significantly higher than those of other samples, but its elongation is the lowest. It can be seen that the work-hardening behavior of ST sample is weakened, and the ultimate tensile strength of ST sample is lower than that of AD sample, while the plasticity is also weakened. The SA sample has the highest ultimate tensile strength but the lowest plasticity among these three samples.

According to Table 1, it can be seen that the elongationand shrinkage of section decrease after heat treatments, compare

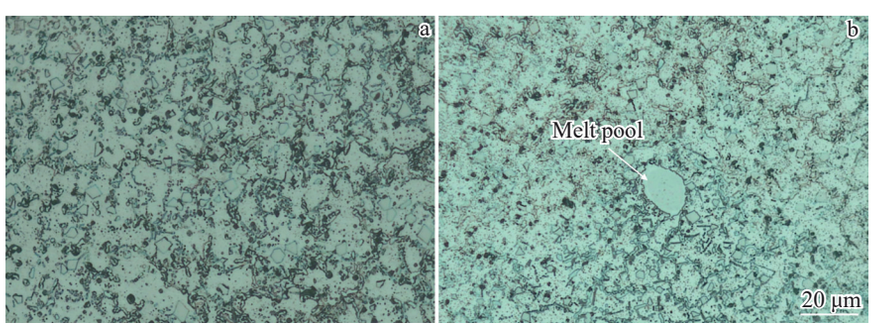


Fig.4 OM microstructures of AD samples at 1115 °C (a) and 1120 °C (b)

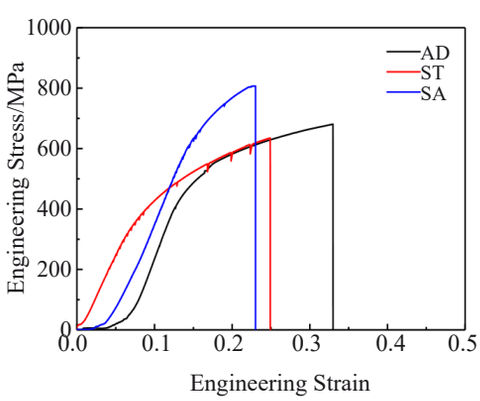


Fig.6 Tensile engineering stress-engineering strain curves of AD, ST, and SA samples at 600 °C

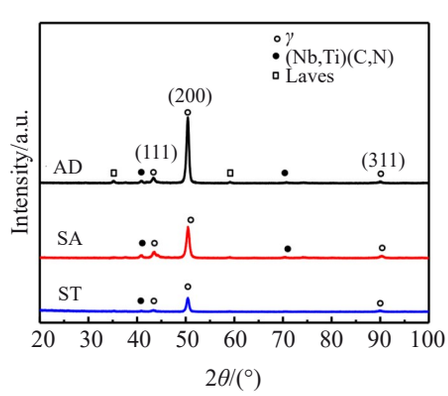


Fig.5 XRD patterns of AD, ST, and SA samples

**Table 1 Mechanical properties of AD, ST, and SA samples after tensile tests at 600 °C**

| Sample | Yield strength, $\sigma_b$/MPa | Ultimate tensile strength, $\sigma_s$/MPa | Elongation, EL/% | Shrinkage of section/% |
|---|---|---|---|---|
| AD | 456.51 | 689.01 | 26.81 | 17.6 |
| ST | 407.04 | 653.74 | 24.97 | 16.3 |
| SA | 535.45 | 811.54 | 23.83 | 15.9 |

with those of AD sample at 600 ℃ . This phenomenon indicates that the solid solution treatment adversely affects the strength and plasticity of the alloys. The ultimate tensile strength of SA sample is higher than that of AD sample by about 120 MPa, while the elongation decreases by approximately 1.1%.

### 3.3 Fracture morphology

The fracture characteristics of the samples of different states after fracture are shown in Fig. 7, and they all show ductile fracture mode. The surface layer of the samples is relatively smooth with shear deformation cleavage surfaces and shallow ductile dimples. The fracture surface of AD sample shows a slight necking characteristic, as shown in Fig. 7a. The fracture morphologies of ST and SA samples are similar to those of AD sample, as shown in Fig. 7b–7c, and the fracture surfaces are flatter in general, but there is no obvious necking phenomenon. There are a large number of ductile dimples at the fracture surface, as shown in Fig. 7d and 7k, accompanied by a small number of tear ribs. The ductile dimples are the typical morphology characteristic of ductile fracture. Fragmented carbide precipitation phases can be observed in the tough dimples of the fracture, as shown in Fig. 7j and 7l. Some slip planes are distributed in the surfaces, as shown in Fig. 7e – 7f, which are usually generated by dislocation slipping along the {111} plane, suggesting that the fracture of the samples may be caused by the stress

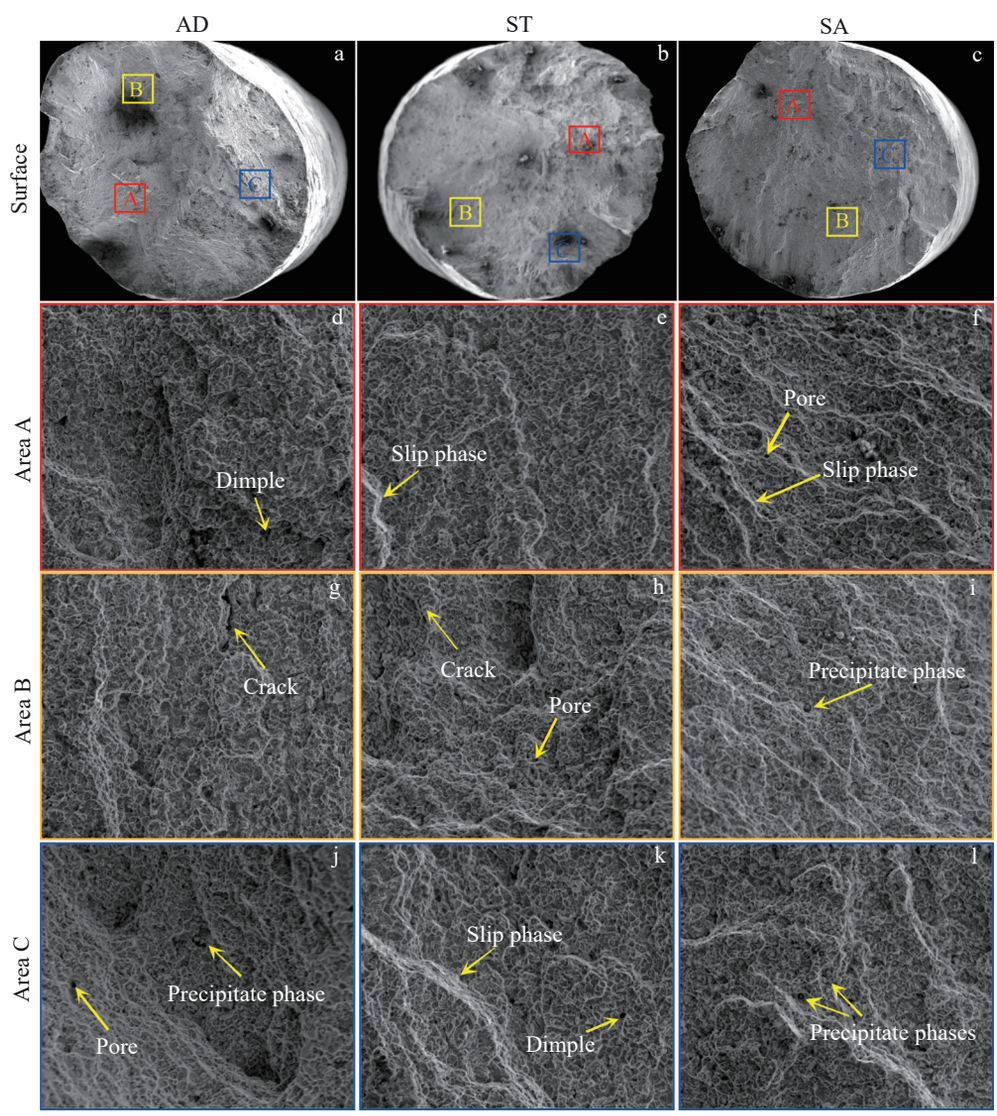


Fig.7 SEM fracture morphologies of AD, ST, and SA samples with magnified images

concentration at the grain boundaries generated by dislocation slipping along the {111} surface[25].

Compared with other samples, some secondary cracks exist in the surface layer of SA sample, as shown in Fig. 7i. The formation of secondary cracks may be due to the concentration of stresses near the reinforcing and carbide phases during plastic deformation, which hinders the movement of dislocations. When the stress concentration exceeds the tensile strength of the alloy, microcracks are produced in the stress concentration region. It is well known that not all microcracks eventually evolve into main cracks. Thus, the brittle fracture and cracked regions in SA sample may be caused by $\gamma'$ phase and intergranular carbide phases[26].

To further explore the crack extension path, the longitudinal-section of the tensile fracture was observed, as shown in Fig. 8. All samples show mixed-mode fracture after tensile tests at 600 °C. The proportion of intergranular cracks in AD sample is larger, and most of the cracks are extended in a mixed pattern mainly along the crystal direction. The proportion of perforated cracks in the samples after heat treatment is larger, most of the cracks are extended in the form of perforated crystals, and some fine cracks can be seen on the longitudinal-section of ST sample. There are also some micropores within the crystal of SA sample, and with the increase in tensile force, these micropores grow and gather together, gradually forming microcracks.

### 3.4 Evolution of microstructure

A large accumulation of dislocations in the matrix channels can be observed in the microstructure of AD sample after tensile fracture at 600 °C, proving that tensile stretching leads to localized deformation of the alloy and the dislocations are unevenly distributed in the microstructure after tensile deformation, as shown in Fig. 9a. Accumulation and entanglement of dislocations can be observed at the grain boundaries, leading to a rapid increase in dislocation density. The solid solution treatment results in the thermally driven forces and the release of distortion energy, thereby leading to the migration of dislocations. Dislocations are entangled near the grain boundaries in ST samples. The dislocation entanglement near grain boundaries forms and is eventually transformed into a cellular structure (Fig. 9b). The microstructure of SA sample shows not only dislocations entangled near grain boundaries, but also laminar dislocations (continuous laminar dislocations) continuously cutting through the matrix channels (Fig. 9c). The dislocations are not uniformly distributed in the microstructure. The presence of laminar dislocations can reduce the density of dislocations accumulated at grain boundaries, which improves the inhomogeneity of dislocation distribution and reduces the possibility of localized deformation in the sample. Therefore, the SA sample should have higher tensile strength, which is consistent with the results of tensile tests.

### 3.5 Precipitation behavior

Fig. 10 shows the distribution of liquid phase elements during the non-equilibrium solidification process of AD sample. It can be seen that the sample is dominated by a grey $\gamma$-Ni matrix with bright precipitation phases distributed between the dendrites. The order of phase transformation in the solidification process is as follows: L→L+$\gamma$→L+$\gamma$+$M$C→L+$\gamma$+$M$C+Laves[27]. In the early stage of solidification, the $\gamma$-Ni phase with fewer solute elements crystallizes firstly, and the L→L+$\gamma$ crystallization process occurs. During solidification of the liquid metal, the solubility of each element in the solid-liquid phase is different. As the solidification reaction proceeds, the alloying elements, such as Mo, Nb, and C, are

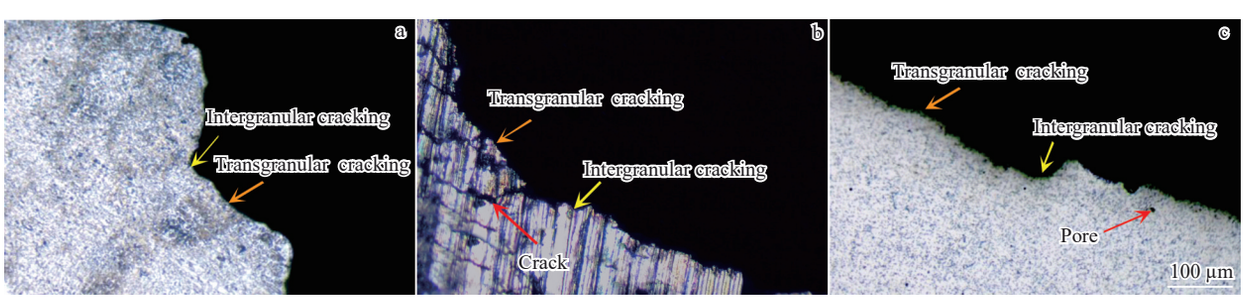


Fig.8 OM images of typical longitudinal-section of fracture surface of AD (a), ST (b), and SA (c) samples after tensile tests at 600 °C

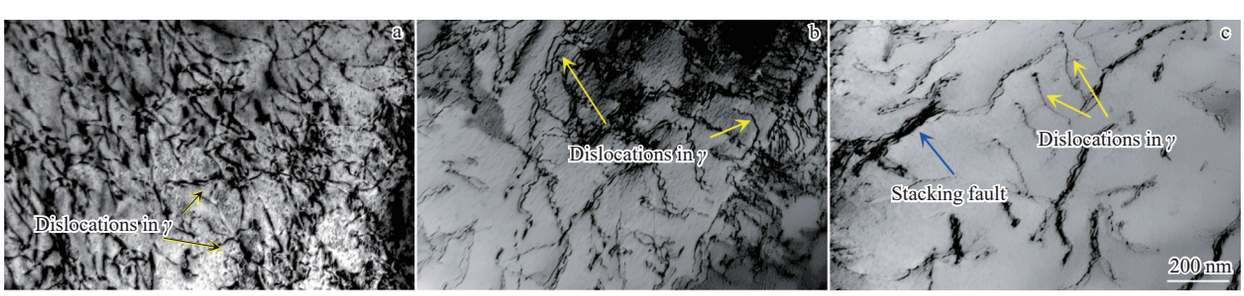


Fig.9 TEM images of deformation microstructures of AD (a), ST (b), and SA (c) samples after tensile tests at 600 °C

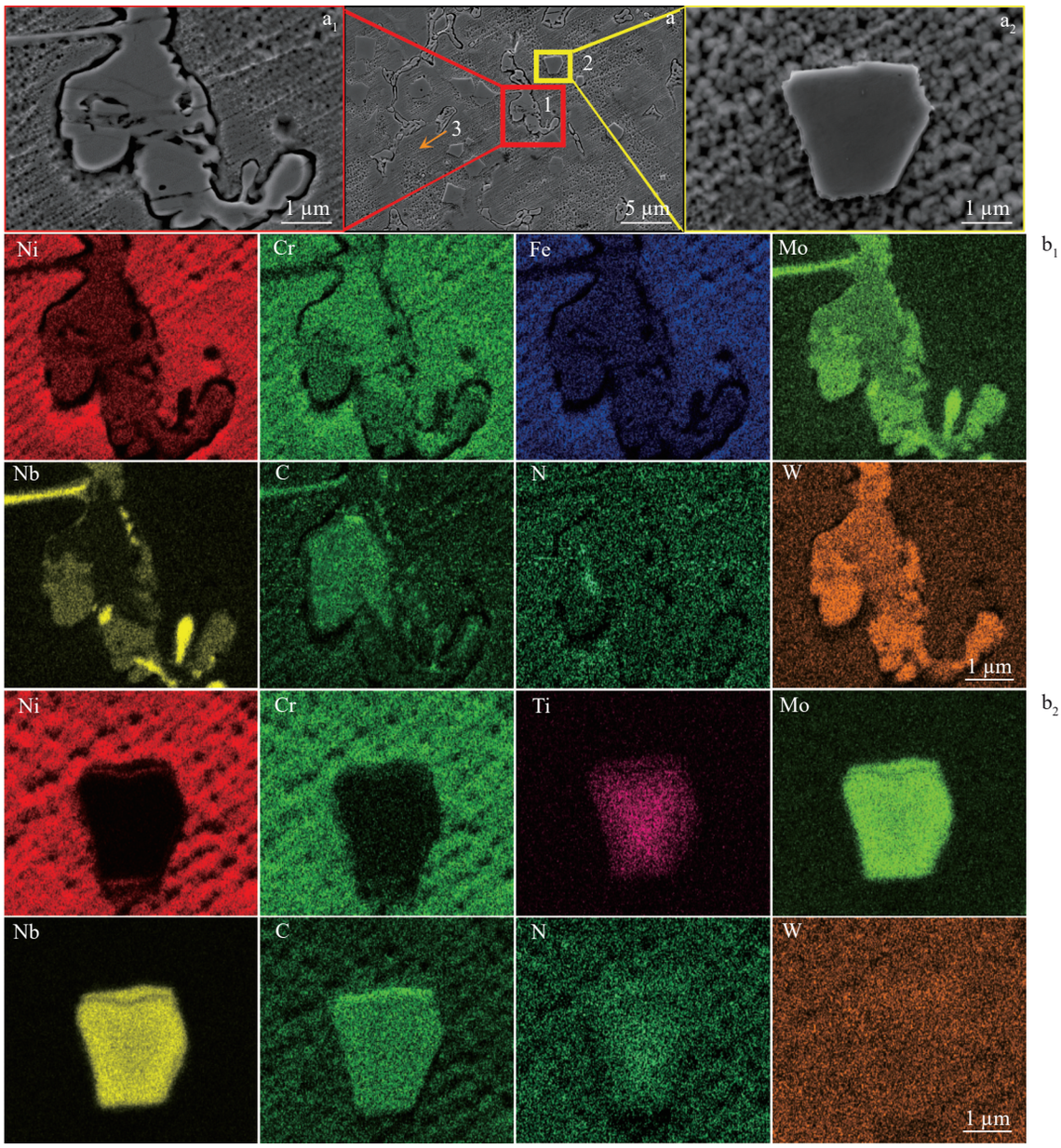


Fig.10 SEM morphologies (a, $a_1$, $a_2$) and EDS element distributions ($b_1$, $b_2$) of AD sample: ($a_1$, $b_1$) results of area 1 in Fig.10a; ($a_2$, $b_2$) results of area 2 in Fig10a

aggregated in the interdendritic region, leading to the segregation behavior of the alloying elements. The occurrence of L→L+$\gamma$+*M*(C, N) promotes the formation of carbonitrides. The Laves phase is a eutectic phase, which forms in the final stage of solidification. In the prepared samples, the precipitation phases at the grain boundaries are irregularly aggregated, and the element distribution result indicates that the precipitation phases are enriched with elements Mo, Nb, Cr, and W. Thus, the deviation of elements Mo, Nb, C, and N in the interdendritic zone leads to the formation of some secondary phases. EDS results of the samples after tensile test at 600 °C are shown in Table 2. The bright phase elements in area 1 in Fig. 10a correspond to the Laves phase of $A_2B$ structure. The bulk phase in area 2 in Fig.10a suggests that the intracrystalline precipitation phase is a carbon-nitride *M*(C, N) composite dominated by Mo and Nb. The results also indicate that the material at point 3 in Fig. 10a is the matrix $\gamma$ phase, mainly containing elements Ni, Cr, and Fe with less contents of other elements.

The distribution characteristics of elements depend on their distribution coefficient (*k*) in the alloy. According to Ref.[28–29], during solidification, when the value of *k* of an element is greater than 1, the element concentration in the solid phase is more intense than that in the liquid phase, indicating that the element concentration in the dendritic crystals is more intense than that in the final solidification region. Conversely, when the *k* value is less than 1, the element concentration in the dendrite is less intense than that in the final solidification region. In this

research, the $k$ values of the elements Ni, Cr, and Fe in the nitrogenous nickel-based AD sample are all greater than 1, ($k_{Ni}$= 1.07; $k_{Cr}$=1.05; $k_{Fe}$=1.23), and the tendency to segregation of Ni and Cr is not obvious. The coefficient of segregation of Fe is the largest, which indicates that the element Fe is more likely to be distributed in the solid phase. The $k$ values of elements Mo, Nb, W, and N are less than 1 ($k_{Mo}$=0.68; $k_{Nb}$=0.50; $k_{W}$=0.75; $k_{N}$= 0.94), which proves that these elements show segregation behavior. Therefore, it can be known that the interdendritic region, which is the final solidified region, will be enriched with a large amount of elements Nb and Mo[30].

Fig. 11a – 11c show SEM morphologies and EDS element distributions of SA sample. Most precipitates have been dissolved into the matrix with a small amount of precipitate remaining at the grain boundaries and within the boundaries. The precipitates mainly contain elements N, C, Nb, and Ti, inferring the $M$(C, N) type carbides. The size of the intracrystalline precipitates in SA sample is smaller than that in AD sample, but sharp edges still exist. The precipitates are more homogeneous after aging, and many small particles are precipitated in the grains, which are proven to be very small $M$(C, N) particles, as indicated by point 2 in Fig. 11d. The

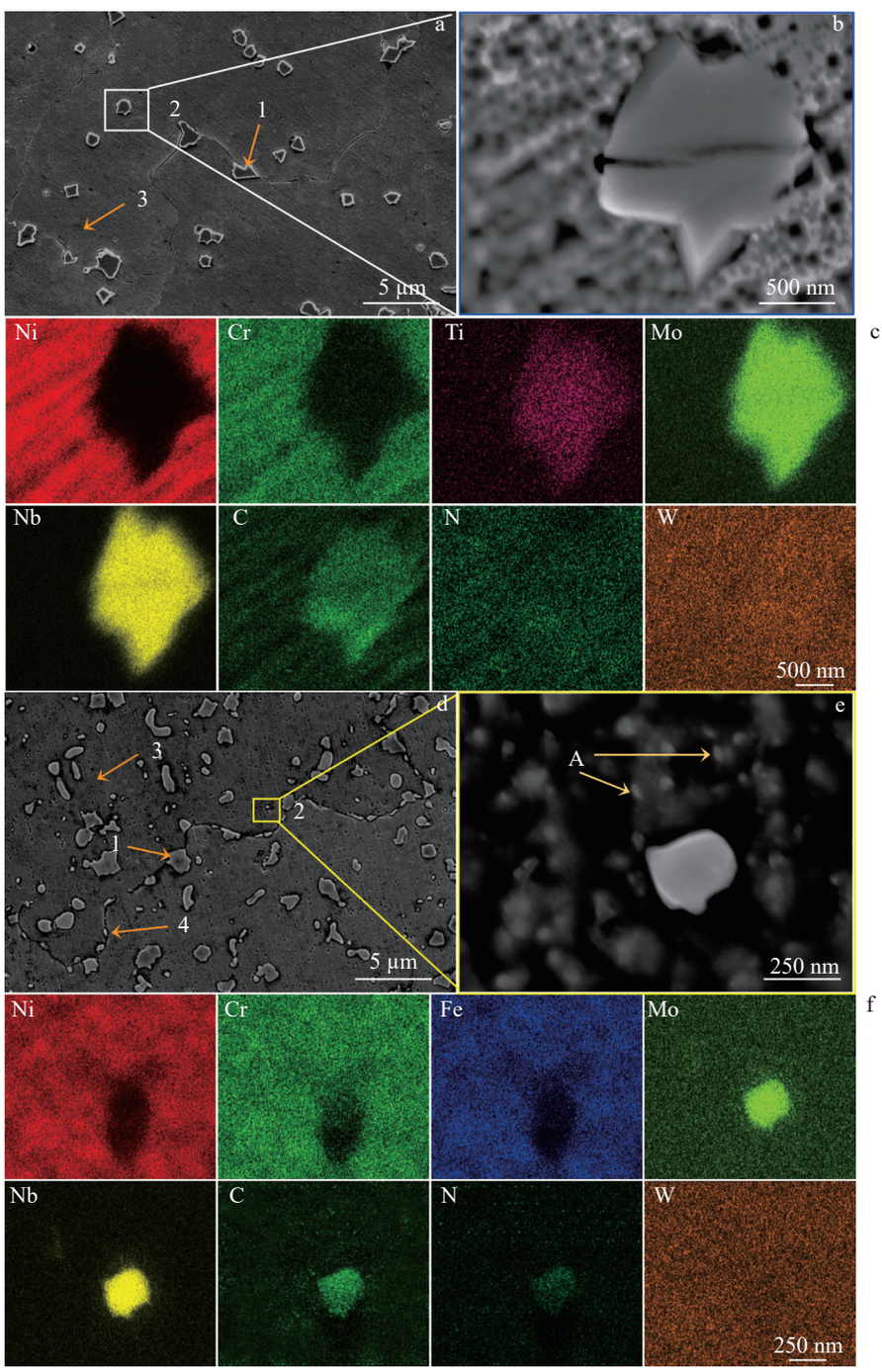


Fig.11 SEM morphologies (a–b, d–e) and EDS element distributions (c, f) of ST (a–c) and SA (d–f) samples

**Table 2 EDS analysis results of different positions marked in Fig.10 and Fig.11 (at%)**

| Sample | Position | Ni | Cr | Fe | Nb | Mo | W | Ti | C | N |
|---|---|---|---|---|---|---|---|---|---|---|
| AD | 1 | 21.1 | 23.3 | 14.3 | 13.3 | 12.5 | 4.9 | 7.4 | 2.4 | 0.8 |
| | 2 | 2.8 | 2.6 | 1.7 | 23.9 | 4.2 | 4.3 | 5.7 | 41.2 | 13.6 |
| | 3 | 40.2 | 25.6 | 23.4 | 1.2 | 1.8 | 2.4 | 0.9 | 0.4 | 2.1 |
| ST | 1 | 2.7 | 2.5 | 1.6 | 23.2 | 3.6 | 6.3 | 4.3 | 41.6 | 15.2 |
| | 2 | 2.6 | 2.3 | 1.6 | 25.1 | 3.8 | 5.9 | 3.6 | 42.6 | 12.5 |
| | 3 | 40.2 | 25.6 | 23.4 | 1.2 | 1.8 | 2.4 | 0.9 | 0.4 | 2.1 |
| SA | 1 | 2.8 | 2.4 | 1.9 | 24.3 | 3.8 | 4.1 | 5.9 | 41.5 | 13.3 |
| | 2 | 2.8 | 2.6 | 1.7 | 23.9 | 4.2 | 4.3 | 5.7 | 41.2 | 13.6 |
| | 3 | 40.5 | 25.3 | 23.1 | 1.5 | 1.8 | 2.2 | 0.8 | 0.6 | 2.2 |
| | 4 | 3.6 | 60.5 | 1.6 | 2.3 | 8.5 | 1.8 | 6.4 | 15.1 | 0.2 |

element analysis results are listed in Table 2. According to Table 2, at the point 3 in Fig. 11d, it is mainly composed of matrix $\gamma$ phase, containing elements Ni, Cr, and Fe with less contents of other elements. It is worth noting that the shape of precipitates in SA sample is more rounded, which reduces the presence of stresses in the grains. At the same time, a nanoscale phase is precipitated in the SA sample, which cannot be detected by XRD, probably due to its low content or the proximity of the lattice to that of the substrate. The precipitation phase at point 4 in Fig. 11d is distributed intermittently along the grain boundary discontinuities, mainly containing elements C, Cr, and Mo. The massive carbides on the grain boundaries significantly reduce, and some granular precipitates appear. Since the molar fraction of C to Cr and W of this precipitate is close to 1:4, the precipitate is presumed to be a $M_{23}C_6$-type carbide. To verify this prediction, TEM and corresponding selected area electron diffraction (SAED) analysis were used for detection, as shown in Fig. 12a. In addition, as shown in Fig. 11e, some ellipsoidal precipitates with size less than 1 μm are distributed within the crystal, and they are further analyzed by TEM, as shown in Fig.12b.

As shown in Fig.12, the precipitates at the grain boundaries are $M_{23}C_6$-type carbides, while the nanoscale ellipsoid-type precipitates within the crystals are $\gamma'$ phases. Since $\gamma$ and $\gamma'$ are crystal structures with similar lattice constants, it is more difficult to accurately determine the constituent elements and ratios of the structures. Besides, the precipitates are more uniformly distributed after aging treatment, and the carbide particles at grain boundaries can retard the mobile dislocations[31]. The abundance of grain boundary diffusion is more favorable to the *M*C decomposition process than the intracrystalline diffusion, so the $M_{23}C_6$ is mainly distributed at grain boundaries or near the grain boundaries[16]. Fine-grained $M_{23}C_6$ can effectively prevent grain boundary migration and strengthen the grain boundaries, while the precipitation of $\gamma'$ phase can effectively improve the yield strength of the material[16,32], which is beneficial to the strength of nickel-based alloys. It can also be found that the element W is enriched in the precipitation phase and matrix. Since element W is also a solid solution strengthening element, it promotes a stronger solid solution strengthening effect, which is one of the reasons leading to the high yield strength of nitrogenous nickel-based alloys.

### 3.6 EBSD analysis

The texture type of nickel-based superalloys is related to process parameters, such as heat input and scanning path. The inverse pole figures (IPFs) and pole figures (PFs) of different samples in *XZ* direction are shown in Fig. 13. It can be seen that the crystals of all samples have a stronger orientation density in the {100} plane, which is consistent with XRD analysis results, i. e., the optimum orientation of the crystal structures is all {100} <100> . This is because the initial solidification stage of the alloy during the preparation process promotes the preferential growth of <100>-oriented grains towards the epitaxial columns, which ultimately leads to the formation of a strong <100> texture in AD sample[33].

The severe segregation during the solidification process leads to the formation of carbides and Laves phases in the interdendritic zone. In addition, directional solidification in the melt pool also leads to anisotropy of mechanical

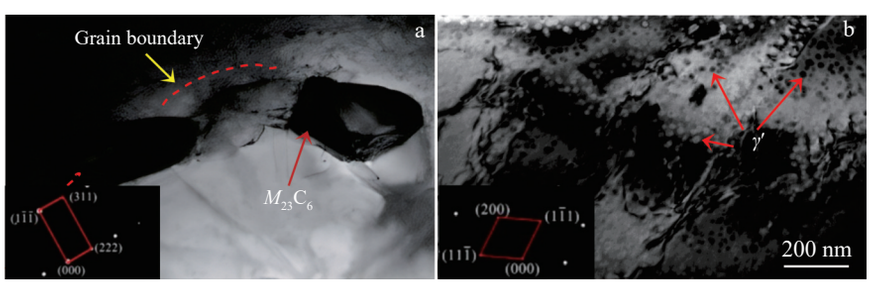


Fig.12 TEM bright field images and SAED patterns of grain boundary (a) and intragranular region (b) in SA sample

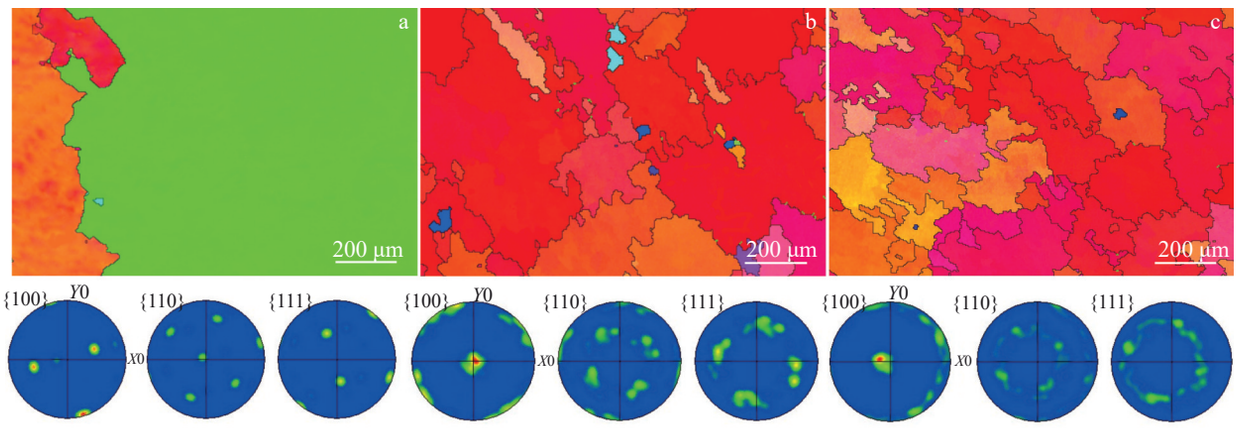


Fig.13 IPFs and PFs of AD (a), ST (b), and SA (c) samples

properties. However, the grain size of the sample becomes smaller after heat treatment, and a large number of equiaxed grains appear, indicating the recrystallization process. The orientation density of ST and SA samples is larger in the {100} plane. This is because the solid solution treatment produces recrystallized grains, eliminating fine dendritic and columnar grains in the samples and forming equiaxed grains, which leads to more isotropic mechanical properties. The grains in SA samples are more uniform.

Fig. 14a – 14c show the local misorientation angle distributions of different samples, which reflects the degree of accumulation of deformation storage energy, and the larger value of local orientation deviation $K$ indicates the higher degree of deformation storage energy[30]. The average values of orientation deviation $K$ of AD, ST, and SA samples are $K_{AD}$ =0.94, $K_{ST}$=0.81, and $K_{SA}$=1.32, respectively. It can be inferred that the SA sample has the highest degree of deformation energy storage, which is consistent with the results in Fig.6.

Fig. 14d – 14f show the distributions of the Schmidt factor of different samples, which reflects the degree of deformation difficulty. The larger the Schmid factor, the easier the slip initiation under a certain external stress. It can be seen that the Schmidt factors of AD and ST samples are distributed in the range of 0.40 – 0.50, whereas the Schmidt factors of SA sample are distributed in the range of 0.37 – 0.50. The average Schmidt factor of AD, ST, and SA samples is 0.45, 0.48, and 0.43, respectively. ST sample has the highest Schmidt factor. Therefore, it can be inferred that ST sample has the lowest mechanical strength among the three samples, whereas the SA sample is expected to have the highest mechanical strength, which is consistent with the results in Fig.6.

## 4 Discussion

Carbide evolution plays an important role in the mechanical properties of nickel-based superalloys[34–35]. Some topologically close-packed phases and metal carbides are formed during the long-term high-temperature exposure, which adversely affects the mechanical properties[36–38]. Carbides are the core of micropore formation[39], and for the nickel-based superalloys, crack sources in the alloys mainly originate from carbides or eutectics[40]. The presence of nitrogen in the alloy leads to the generation of intracrystalline carbon-nitrides with enhanced intracrystalline strengthening, which are more stable than carbides[14]. The eutectic and carbon-nitride compounds of AD sample are predominantly distributed between the dendrites. The size of the precipitates at the grain boundaries is larger than the size of eutectic within the crystals (Fig. 9). As a result, cracks mainly start at grain boundaries, thus promoting the fracture of alloy along the grain in the deformation process with a mixed fracture mechanism. In addition, the element W added to the alloy is enriched in the precipitation phase and the matrix, so the alloy has a stronger solid solution strengthening effect. Precipitation phases at the grain boundaries of samples after heat treatment are dissolved or mostly remelted into the matrix (Fig. 10), and cracks are initiated at the edges of the intracrystalline precipitation phases, which leads to fracture of the alloy in high-temperature deformations by a mixed fracture mechanism dominated by the penetration of crystals. Matrix-strengthened precipitates during the aging process lead to a reduction in the elongation and cross-sectional shrinkage of the sample, and $M$C-type carbide particles can cause a deterioration in ductility at elevated temperatures[32]. The high yield strength of the SA sample can be attributed to the following factors. (1) Finer grain size and more uniform precipitation of strengthening phases. Fig. 10 shows that the intragranular precipitates in the SA sample are smaller in size and have different shapes, which change from block-like shape in AD state to the ellipsoidal shape, weakening the stress concentration. (2) Most $M$C-type carbides on the grain boundaries redissolve into the matrix, exerting a solid solution strengthening effect. $M_{23}C_6$ on the grain boundaries prevents the sliding of grain boundaries, so the strength of the alloy is improved[16–17]. (3) The presence of nitrogen in the alloy leads to the generation of a large amount of carbon-nitride within the grains, which is more stable than carbides[14], and the

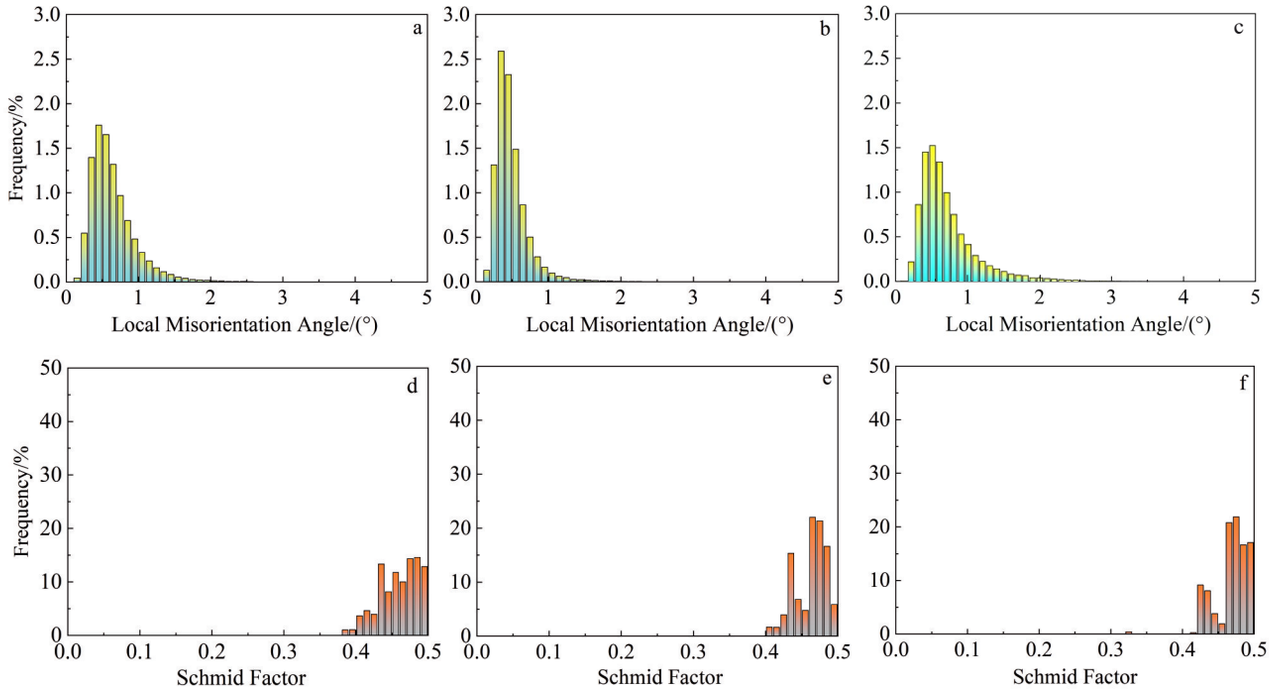


Fig.14 Local misorientation angle distributions (a–c) and Schmid factor distributions (d–f) of AD (a, d), ST (b, e), and SA (c, f) samples

intragranular strengthening effect is enhanced. (4) A large number of $\gamma'$ strengthening phases are present. As a result, the nitrogenous nickel-based alloys after aging treatment have high yield strength but low plasticity. The precipitates in the ST sample are large in size and irregular in shape, and the angular precipitates can easily become the source of stress concentration (Fig. 10a). Thus, the mixed fracture occurs through crystal. Since no precipitation phase exists at the grain boundaries to exert the pinning effect, the precipitates change the shape of grain boundaries into more zigzag one and avoid grain boundary sliding[41–42]. Therefore, the strength of the solid-solution-treated sample is inferior.

A microstructure development model is proposed based on the microstructure evolution of AD, ST, and SA samples, as shown in Fig. 15. It is particularly important to release segregated elements and reduce entangled vortex structures. Aging treatment after solid solution treatment promotes the formation of intergranular $M_{23}C_6$ carbides and $\gamma'$ strengthening phase, and it also induces the precipitation of fine secondary carbide structures, which is particularly prominent for the strengthening effect.

Through Oxford HKL Channel 5 software, it can be seen that the SA sample has a more uniform grain microstructure. Based on the local misorientation angles of the three samples, it can be inferred that the SA sample has the highest degree of deformation energy storage, while the ST sample has the lowest deformation energy storage. By calculating the average Schmid factor of three samples, it is found that the Schmid factor of the ST sample is the highest, while that of the SA sample is the lowest. In a specific slip system, the larger the Schmid factor, the easier the slip initiation under external stress. Larger Schmid factors are more likely to cause grain deformation[30]. Therefore, it can be inferred that the ST sample has the lowest mechanical strength among three samples, whereas the SA sample has the highest mechanical strength. These conclusions are also consistent with the results of the tensile tests.

Plastic fracture damage is the result of a combination of local necking and microporous aggregation under various deformation conditions. After tensile fracture, the alloy section becomes wedge-shaped, and some slip surfaces can also be observed. For polycrystalline nickel-based alloys, there are orientation deviations between different grains, so different slip systems are initiated within different grains during plastic deformation. Dislocations and laminations within different grains slip along the {111} surface and eventually accumulate near the grain boundaries, causing stress concentration at the grain boundaries. With the accumulation of tensile deformation, the stress concentration at grain boundaries gradually increases. When the stress concentrated at the grain boundary exceeds the strength of the grain boundary, it will lead to the formation of cracks along the grains. With the increase in temperature during heat treatment, the precipitation phase gradually dissolves back into the matrix, and the microscopic deformation mechanism changes from dislocation cutting the precipitation phase system to dislocation sliding and climbing, and the stress concentration at the grain boundary can be ameliorated.

Entangled dislocations are observed in the microstructure of all three samples after fracture. Since the transition group elements Co and W are added to the nitrogenous nickel-based flux-cored wires to reduce the layer dislocation energy of the

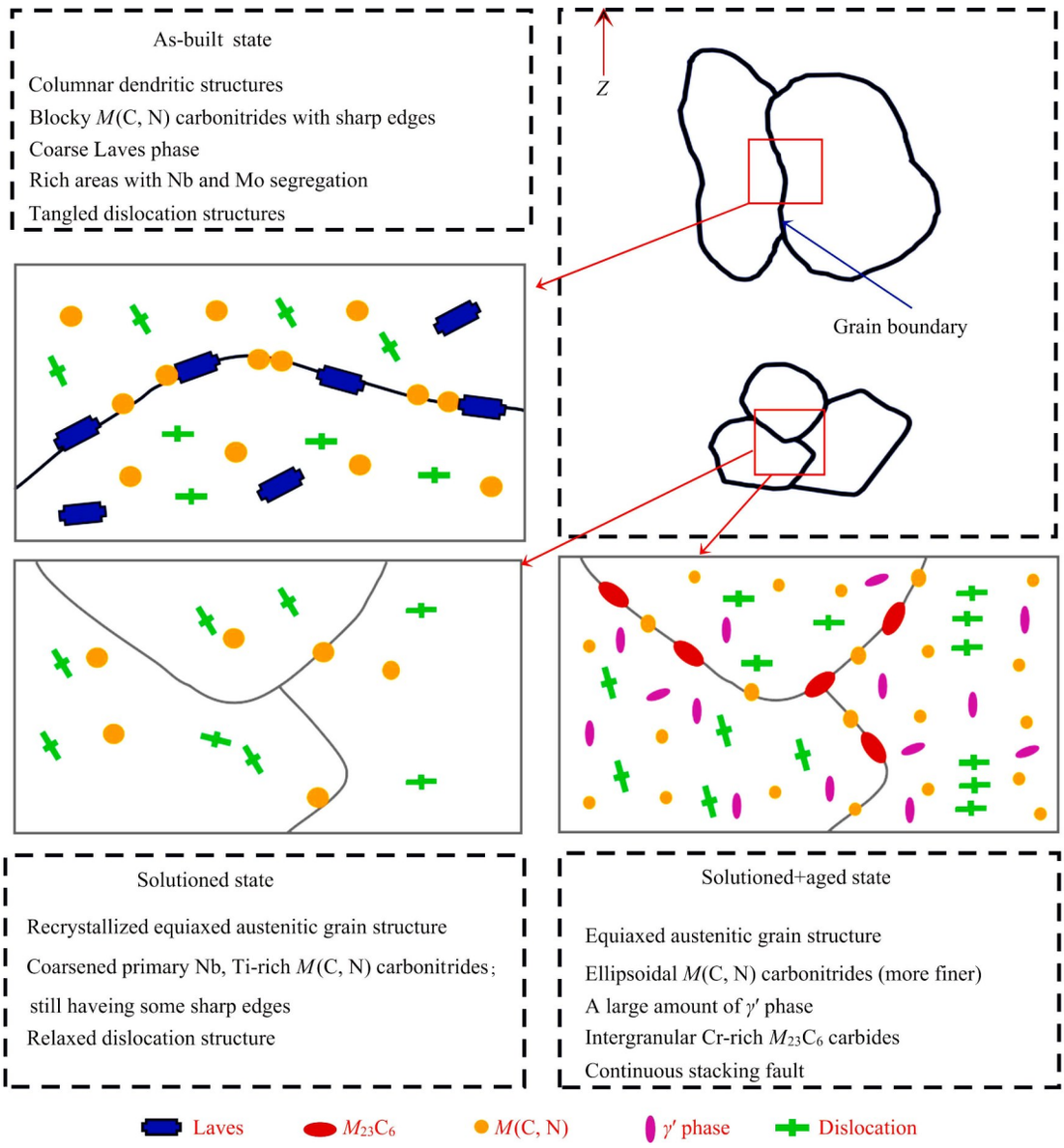


Fig.15 Schematic diagrams of major microstructure evolutions in nitrogenous nickel-based deposited metal fabricated by GMAW after different heat treatment stages

alloys[11,43], the nitrogenous nickel-based alloys have lower layer dislocation energies, which are favorable to the formation of layer dislocations. In the ST sample, some dislocation entanglement and a small amount of dislocation accumulation in the matrix channel can be observed. In the SA sample, some entangled dislocations can be observed in the matrix, forming a substructure. Many laminar dislocations can also be observed, exerting the hindering effect on dislocation slip and providing a work-hardening effect. It is suggested that laminar dislocations are formed by the decomposition of the matrix dislocation $a/2<101>$ into $a/6<121>$ Shockley incomplete dislocation and $a/3<112>$ leading dislocation at the interface of the matrix and the precipitation phase after $a/3<112>$ cuts the precipitation phase[44]. Ref. [45] reported that layer dislocations are formed by two Shockley incomplete dislocations together cutting the precipitation phase. Regardless of the dislocation theory, it is a stacking fault left behind by an overtopping incomplete dislocation cutting the precipitation phase. If the dislocations continue to slip, a continuous stacking fault is formed.

Research shows that the fracture mode of nickel-based alloys at 600 °C is mainly mixed fracture with intergranular fracture[46]. This is due to the overall wedge shape with the presence of some sliding surfaces of the cross-section of alloy in this temperature interval. For polycrystalline nickel-based alloys, there are orientation deviations between different grains. Alloys undergo plastic deformation by inducing different slip systems within different grains. Dislocations and stacking faults within different grains slide along the {111} plane and gather near grain boundaries, resulting in stress concentration at the grain boundaries. With the accumulation of tensile deformation, intergranular cracking occurs when the

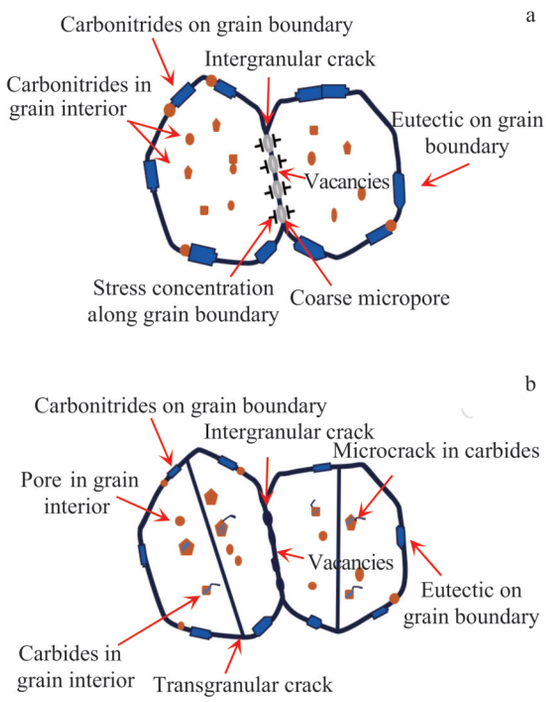


Fig.16 Fracture models in medium-to-low temperature zone (a) and high temperature zone (b)

concentrated stress at the grain boundaries increases to a certain level exceeding the strength of the grain boundaries. The crack source of nickel-based superalloys usually originates from the carbides or eutectic sites[15]. The size of carbides at grain boundaries in this research is larger than the size of eutectics within the grains (Fig.10–Fig.11). Therefore, cracks mainly originate from grain boundaries with the intergranular fracture mechanism as the main mechanism. Fig. 16 shows the models of intergranular crack propagation. In addition, stress and strain rate also have a certain influence. The strain rate in the tensile test remains constant, whereas the rheological stress varies with temperature. When the rheological stress is at a high level, the coordination ability between grain boundaries cannot keep up with the deformation inside the grains. Sliding occurs between grain boundaries, resulting in intergranular cracks.

## 5 Conclusions

1) The microstructure of the nitrogenous nickel-based cladding metal is mainly composed of epitaxial growth of columnar grains. The alloy has large grains with internal massive carbon-nitride generation. Due to the precipitation of elements Nb and Mo between the dendrites, a clustered Laves phase is formed between the dendrites in the final solidification stage. The Laves phase of ST sample completely dissolves into the matrix, and the carbides partially dissolve. $M_{23}C_6$ carbides form at grain boundaries in SA sample, as well as a small number of elongated Laves phases. Nanoscale *M*(C, N) and a large amount of $\gamma'$ phase are precipitated within the grains.

2) After solid solution and aging treatments, the alloy undergoes static recrystallization, and the coarse grains are replaced by the equiaxed crystals. The heat-treated samples have finer and more uniform grains with a stronger <100> solidification texture. The average orientation deviations of AD, ST, and SA samples are 0.94, 0.81, and 1.32, respectively.

3) The yield strength and ultimate tensile strength of AD sample are 456.51 and 689.01 MPa, respectively, and the elongation is 26.81%. After the solid solution treatment, the yield strength and elongation reduce. A large number of $\gamma'$ phases form in the SA sample, the nanoscale *M*(C, N) is precipitated in the crystal, and $M_{23}C_6$ phases exist at the grain boundaries, which all greatly increase the strength of the alloys. But the elongation reduces.

## References

1 Pavan A H V, Vikrant K S N, Ravibharath R *et al*. *Materials Science and Engineering A*[J], 2015, 642: 32
2 Jang C, Lee J, Sung K J *et al*. *International Journal of Pressure Vessels and Piping*[J], 2008, 85(9): 635
3 Kumar N P, Shanmugam N S, Sreedhar G. *Surface and Coatings Technology*[J], 2021, 415: 127138
4 Guo Longlong, Zheng Hualin, Liu Shaohu *et al*. *Rare Metal Materials and Engineering*[J], 2016, 45(9): 2219 (in Chinese)
5 Corigliano P, Crupi V. *Ocean Engineering*[J], 2021, 221: 108582
6 Shang S L, Kim D E, Zacherl C L *et al*. *Journal of Applied Physics*[J], 2012, 112: 053515
7 Lin Y, Wang C. *Computational Materials Science*[J], 2021, 195: 11044
8 Duhl D N, Sullivan C P. *Journal of Metals*[J], 1971, 23(7): 38
9 Eriş R, Akdeniz M V, Mekhrabov A O. *Metallurgical and Materials Transactions A*[J], 2022, 53: 1859
10 Zhao Ning, Tao Li, Guo Hui *et al*. *Rare Metal Materials and Engineering*[J], 2018, 47(1): 20
11 Sengupta A, Putatunda S K, Bartosiewicz L *et al*. *Journal of Materials Engineering and Performance*[J], 1994, 3(1): 73
12 Chookajorn T, Heather A. Murdoc C A. *Science*[J], 2012, 337(6097): 951
13 Kermanpur A, Behjati P, Han J *et al*. *Materials & Design*[J], 2015, 82: 273
14 Fox S, Brooks J W, Loretto M H *et al*. *Strength of Metals and Alloys*[M]. Pergamon: ICSMA, 1985: 399
15 Liu T, Dong J S, Wang L *et al*. *Journal of Materials Science & Technology*[J], 2015, 31(3): 269
16 He L Z, Zheng Q, Sun S F *et al*. *Journal of Materials Science*[J], 2005, 40: 2959
17 Huang Xuebing, Kang Yan, Zhou Huihua *et al*. *Materials Letters*[J], 1998, 36(1–4): 210
18 Qin X Z, Guo J T, Yuan C *et al*. *Materials Science and Engineering A*[J], 2008, 485(1–2): 74
19 Sajad Ghaemifar, Hamed Mirzadeh. *Journal of Materials*

*Research and Technology*[J], 2023, 24: 3491
20 Qin X Z, Guo J T, Yuan C *et al*. *Metallurgical and Materials Transactions A*[J], 2007, 38(11): 3014
21 Abolfazl S, Mahmood S, Mahdi S A. *Transactions of Nonferrous Metals Society of China*[J], 2020, 30(11): 3016
22 Mathieu T, Lee J, Giulio M *et al*. *Materials*[J], 2020, 13(20): 4643
23 Wang Huan, Wu Daijian, Xiao Feng *et al*. *Materials Today Communications*[J], 2024, 14: 110673
24 Mostafaei A, Behnamian Y, Krimer Y L *et al*. *Materials & Design*[J], 2016, 111: 482
25 Chu Zhaokuang, Yu Jinjiang, Sun Xiaofeng *et al*. *Metallurgical and Materials Transactions A*[J], 2009, 40: 2927
26 Giulio Marchese, Massimo Lorusso, Simone Parizia *et al*. *Materials Science and Engineering A*[J], 2018, 729: 64
27 Hu Yunlong, Lin Xin, Li Yunlong *et al*. *Materials Science and Engineering A*[J], 2021, 817: 141309
28 DuPont J N. *Metallurgical & Materials Transactions A*[J], 1996, 27: 3612
29 Khajavi L T, Morita K, Yoshikawa T *et al*. *Metallurgical and Materials Transactions B*[J], 2015, 46: 615
30 Zhao T, Zhang S, Wang Z Y *et al*. *Wear*[J], 2022, 510–511: 204510
31 Yu Jinjiang, Lian Zhanwei, Chu Zhaokuang *et al*. *Materials Science and Engineering A*[J], 2010, 527: 1896
32 Appa R A, Mahendra K, Srinivas M *et al*. *Materials Science and Engineering A*[J], 2003, 355(1–2): 114
33 Dinda G P, Dasgupta A K, Mazumder J *et al*. *Scripta Materialia*[J], 2012, 67(5): 503
34 Heo N H, Chang J C, Kim S J. *Materials Science and Engineering A*[J], 2013, 559: 665
35 Roy A K, Pal J, Mukhopadhyay C. *Materials Science and Engineering A*[J], 2008, 474(1–2): 363
36 Tang L, Guo Q, Li C *et al*. *Journal of Materials Science & Technology*[J], 2022, 128: 180
37 Krakow R, Johnstone D N, Eggeman A S *et al*. *Acta Materialia*[J], 2017, 130: 271
38 Vishwakarma K R, Richards L N, Chaturvedi M C. *Materials Science and Engineering A*[J], 2008, 480: 517
39 Lin Y C, Deng J, Jiang Y Q *et al*. *Materials & Design*[J], 2014, 55: 949
40 Du Beining, Yang Jinxia, Cui Chuanyong *et al*. *Materials Science and Engineering A*[J], 2015, 623: 59
41 Ramirez A J, Lippold J C. *Materials Science and Engineering A*[J], 2004, 380(1–2): 259
42 Ramirez A J, Lippold J C. *Materials Science and Engineering A*[J], 2004, 380(1–2): 245
43 Yang Nanseng, Wei Yuhuan, Fu Hongzheng *et al*. *Acta Metallurgica Sinica*[J], 1981, 17(1): 44
44 Rae C M F, Reed R C. *Acta Materialia*[J], 2007, 55(3): 1067
45 Viswanathan G B, Sarosi P M, Henry M F *et al*. *Acta Materialia*[J], 2005, 53(10): 3041
46 Dai Zhiyong, Su Yunhai, Wang Yingdi *et al*. *Materials Science and Engineering A*[J], 2024, 903: 146671

# 从焊态到热处理态的新型含氮镍基熔敷金属显微组织演变特征及力学性能

王英第[1,2]，张桂清[1]，杨太森[1]，梁学伟[1]，苏允海[1]
(1. 沈阳工业大学 材料科学与工程学院，辽宁 沈阳 110870)
(2. 烟台职业学院 交通工程系，山东 烟台 264670)

**摘　要：**采用气体保护金属极弧焊制备了新型含氮镍基熔敷金属，然后分别对其进行固溶处理、固溶和时效处理。研究了不同状态下的熔覆金属微观结构和拉伸性能的变化。结果表明，添加W和N元素后，沉积金属的高温抗拉伸强度表现良好。合金样品的晶粒尺寸较大，且在晶界处出现了花瓣状的Laves相。固溶处理后的样品晶粒尺寸减小，Laves相消失，但金属的屈服强度和伸长率都有所下降。固溶和时效处理后的样品晶粒尺寸更加均匀，晶体内析出了纳米级$M$(C, N)相，晶界处形成了$M_{23}C_6$相，样品的屈服强度和极限抗拉伸强度均高于其他样品，但塑性最低。主要变形机制是单位位错$a$/2<110>切削析出相。

**关键词：**含氮沉积金属；显微结构；拉伸性能；位错

作者简介：王英第，女，1987年生，博士生，沈阳工业大学材料科学与工程学院，辽宁 沈阳 110870，E-mail：wyy150403@163.com